

# Antiferromagnetism in trigonal $\text{SrMn}_2\text{As}_2$ and $\text{CaMn}_2\text{As}_2$ single crystals

N. S. Sangeetha, Abhishek Pandey,\* Zackery A. Benson, and D. C. Johnston†

Ames Laboratory and Department of Physics and Astronomy, Iowa State University, Ames, Iowa 50011, USA

(Dated: June 15, 2019)

Crystallographic, electronic transport, thermal and magnetic properties are reported for  $\text{SrMn}_2\text{As}_2$  and  $\text{CaMn}_2\text{As}_2$  single crystals grown using Sn flux. Rietveld refinements of powder x-ray diffraction data show that the two compounds are isostructural and crystallize in the trigonal  $\text{CaAl}_2\text{Si}_2$ -type structure (space group  $P\bar{3}m1$ ), in agreement with the literature. Electrical resistivity  $\rho$  versus temperature  $T$  measurements demonstrate insulating ground states for both compounds with activation energies of 85 meV for  $\text{SrMn}_2\text{As}_2$  and 61 meV for  $\text{CaMn}_2\text{As}_2$ . In a local-moment picture, the  $\text{Mn}^{+2} 3d^5$  ions are expected to have high-spin  $S = 5/2$  with spectroscopic splitting factor  $g \approx 2$ . Magnetic susceptibility  $\chi$  and heat capacity measurements versus  $T$  reveal antiferromagnetic (AFM) transitions at  $T_N = 120(2)$  K and 62(3) K for  $\text{SrMn}_2\text{As}_2$  and  $\text{CaMn}_2\text{As}_2$ , respectively. The anisotropic  $\chi(T \leq T_N)$  data indicate that the hexagonal  $c$  axis is the hard axis and hence that the ordered Mn moments are aligned in the  $ab$  plane. The  $\chi(T)$  data for both compounds show strong dynamic short-range AFM correlations up to at least 900 K, evidently associated with quasi-two-dimensional connectivity of strong AFM exchange interactions between the Mn spins within the corrugated honeycomb Mn layers parallel to the  $ab$  plane.

PACS numbers: 75.50.Ee, 74.70.Xa, 75.40.-s, 72.15.Eb

## I. INTRODUCTION

The body-centered tetragonal  $AM_2X_2$  ternary compounds ( $A$  = rare or alkaline earth,  $M$  = transition metal,  $X$  = Si, Ge, P, As, Sb) with the  $\text{ThCr}_2\text{Si}_2$  structure<sup>1</sup> have generated tremendous interest in the scientific community due to their novel electronic and magnetic properties. Prominent among these are the iron-arsenide family of parent compounds  $A\text{Fe}_2\text{As}_2$  ( $A$  = Ca, Sr, Ba, Eu).<sup>2–10</sup> These materials are metallic and show nearly contiguous antiferromagnetic (AFM) spin-density wave and structural transitions at temperatures  $T$  up to  $\sim 200$  K. The suppression of these transitions by external pressure or chemical doping leads to superconductivity with maximum bulk superconducting transition temperatures  $T_c$  up to 56 K. It is believed that the FeAs layer as the conducting sheet in this structure plays a crucial role in the occurrence of superconductivity.<sup>2–10</sup> Hence, it is important to investigate other related materials with similar compositions and structures in the search for new superconductors and other novel phenomena. For example,  $\text{SrNi}_2\text{As}_2$  ( $T_c = 0.62$  K, Ref. 11) and  $\text{BaNi}_2\text{As}_2$  ( $T_c = 0.7$  K, Ref. 12) were both found to be superconductors.

On the other hand,  $\text{SrCo}_2\text{As}_2$  (Refs. 13–15) and  $\text{BaCo}_2\text{As}_2$  (Refs. 16,17) are correlated metals with no structural, superconducting or long-range magnetic ordering transitions. From inelastic neutron scattering measurements,  $\text{SrCo}_2\text{As}_2$  is found to exhibit strong AFM correlations at the same stripe wavevector as do the superconducting iron arsenides, which raises the interesting question of why  $\text{SrCo}_2\text{As}_2$  is not a high- $T_c$  superconductor.<sup>14</sup> The reason has been suggested from NMR measurements to be that  $\text{SrCo}_2\text{As}_2$  exhibits strong *ferromagnetic* (FM) spin correlations/fluctuations in addition to the AFM correlations and these compete with

the AFM correlations that are the presumptive glue for superconductivity in these systems. Subsequent NMR studies indicated that the large range of  $T_c$  observed within the FeAs-based systems may also arise from the competition between FM and AFM correlations.<sup>18</sup>

Recently significant attention has focussed on Mn arsénides. Our studies of the properties of the parent and doped  $\text{BaMn}_2\text{As}_2$  systems were originally motivated by their potential to be  $\text{ThCr}_2\text{Si}_2$ -type high- $T_c$  superconductors analogous to the cuprates. The semiconductor  $\text{BaMn}_2\text{As}_2$  shows G-type (checkerboard-type) local-moment collinear AFM order below its high Néel temperature  $T_N = 625$  K with the ordered moments aligned along the tetragonal  $c$  axis.<sup>19–21</sup> Thus magnetoelastic coupling does not cause a distortion of the crystal structure below  $T_N$ , contrary to the orthorhombic distortion associated with AFM ordering in the  $A\text{Fe}_2\text{As}_2$  compounds due to the collinear Fe ordered moments aligned in the  $ab$  plane. An optical gap of 48 meV was inferred for  $\text{BaMn}_2\text{As}_2$  from the optical conductivity,<sup>22</sup> consistent with results from the electrical resistivity  $\rho$  versus temperature  $T$  measurements in the  $ab$  plane.<sup>19</sup> Furthermore, this optical study<sup>22</sup> found that  $\text{BaMn}_2\text{As}_2$  is much more two-dimensional in its electronic properties than are the  $A\text{Fe}_2\text{As}_2$  parent compounds.<sup>19</sup> A neutron scattering study of isostructural  $\text{BaMn}_2\text{Bi}_2$  found the same G-type AFM structure as in  $\text{BaMn}_2\text{As}_2$  but with a lower  $T_N = 387$  K.<sup>23</sup>

Only 1.6% K substitution for Ba transforms  $\text{BaMn}_2\text{As}_2$  into a local-moment AFM metal.<sup>24,25</sup> Higher doping levels lead to the onset of FM at  $\approx 16\%$  K-doping<sup>26</sup> and half-metal FM behavior below the Curie temperature  $T_C \sim 100$  K at 40% K doping (Refs. 27,28) and at 60% Rb doping.<sup>29</sup> The FM is thus thought to be associated with FM ordering of the itinerant doped-hole spins and coexists with the G-type AFM order of the local Mn mo-

ments with  $T_N > 300$  K.<sup>28,30</sup>

Unlike  $\text{BaMn}_2\text{As}_2$  with the tetragonal  $\text{ThCr}_2\text{Si}_2$  structure, the compounds  $\text{SrMn}_2\text{As}_2$  and  $\text{CaMn}_2\text{As}_2$  both crystallize in the trigonal  $\text{CaAl}_2\text{Si}_2$ -type structure<sup>31,32</sup> containing a buckled honeycomb Mn sublattice which can be viewed as a triangular lattice bilayer. The possibility of geometrically-frustrated triangular-lattice exchange connectivity exists and such compounds often show novel physical behaviors associated with the geometric frustration.<sup>33–35</sup> Single crystals of  $\text{SrMn}_2\text{As}_2$  were grown previously using Sn flux.<sup>36</sup> These authors' in-plane electrical resistivity  $\rho(T)$  measurements indicated that the ground state is insulating with activation energies of 0.29–0.64 eV depending on the  $T$  range, and their magnetic susceptibility  $\chi(T)$  measurements indicated an AFM transition at  $T_N = 125$  K.<sup>36</sup>

Two neutron powder diffraction studies<sup>37,38</sup> of the related  $\text{CaAl}_2\text{Si}_2$ -type  $\text{CaMn}_2\text{Sb}_2$  revealed AFM ordering below  $T_N = 88$  K and 85 K, respectively, with an AFM propagation vector  $\mathbf{k} = (0, 0, 0)$ , i.e., the crystal and AFM unit cells are the same. In the former paper the AFM structure was deduced to be collinear, with the ordered moments aligned in the  $ab$  plane with a low- $T$  ordered moment of  $2.8(1)$   $\mu_B/\text{Mn}$ , where  $\mu_B$  is the Bohr magneton. In the latter paper, a model was favored with the ordered moments canted at  $\pm 25^\circ$  with respect to the  $ab$  plane with an ordered moment of  $3.38(6)$   $\mu_B/\text{Mn}$ .

Herein, we report the growth, crystal structure,  $\rho(T)$ , magnetization as a function of magnetic field  $M(H)$ ,  $\chi(T)$  and heat capacity  $C_p(T)$  measurements of  $\text{CaMn}_2\text{As}_2$  and  $\text{SrMn}_2\text{As}_2$  single crystals. These studies were initiated because of the above-noted possibility that the Mn spin lattice might exhibit novel magnetic behaviors associated with the presence of geometric frustration within the triangular-lattice Mn layers. If the strongest AFM interactions are indeed within a triangular lattice layer, this should lead to a noncollinear AFM structure below  $T_N$ . Instead, in a companion neutron diffraction study to the present work, the AFM structure of  $\text{SrMn}_2\text{As}_2$  was found to be collinear with the ordered Mn moments aligned in the  $ab$  plane with magnitude  $3.6$   $\mu_B/\text{Mn}$ .<sup>39</sup> This magnetic structure is the same as one of the two AFM structures proposed for  $\text{CaMn}_2\text{Sb}_2$  (Ref. 37) discussed above.

However, in the course of the present study, we found that the  $\chi(T)$  of  $\text{SrMn}_2\text{As}_2$  and  $\text{CaMn}_2\text{As}_2$  above their respective Néel temperatures  $T_N$  of 120 and 62 K exhibit behaviors characteristic of strong dynamic short-range AFM spin correlations up to at least 900 K, evidently arising from quasi-two-dimensional connectivity of strong AFM Mn–Mn exchange interactions within the corrugated honeycomb Mn spin sublattice. This result is exciting because such strong AFM spin correlations up to high temperatures and the suppression of  $T_N$  to much lower temperatures than expected from molecular field theory, due to quantum fluctuations associated with the low dimensionality of the exchange interaction connectivity, may give rise to interesting physical properties upon

doping the compounds into the metallic state.

## II. EXPERIMENTAL DETAILS

Single crystals of  $\text{SrMn}_2\text{As}_2$  and  $\text{CaMn}_2\text{As}_2$  were grown using Sn flux. High-purity elements Sr (99.95%) from Sigma Aldrich, and Ca (99.95%), Co (99.998%), As (99.9999%) and Sn (99.999%) from Alfa Aesar were taken in the ratio (Sr,Ca):Mn:As:Sn = 1:2:2:20 and placed in an alumina crucible that was subsequently placed in a silica tube that was evacuated, partially refilled with high-purity argon ( $\approx 1/4$  atm pressure) and then sealed. After preheating at 600 °C for 5 h, the assembly was heated to 1150 °C at the rate of 50 °C/h and held at this temperature for 20 h for homogenization. Then the furnace was slowly cooled at the rate of 5 °C/h to 700 °C. At this temperature the molten Sn flux was decanted using a centrifuge. Several shiny hexagonal-shape single crystals of maximum dimensions  $4 \times 3 \times 1$  mm<sup>3</sup> were obtained.

Semiquantitative chemical analyses of the single crystals were performed using a JEOL scanning electron microscope (SEM) equipped with an EDX (energy-dispersive x-ray analysis) detector, where a counting time of 120 s was used. A room-temperature powder x-ray diffraction (XRD) pattern was recorded on crushed single crystals using a Rigaku Geigerflex powder diffractometer with Cu  $K\alpha$  radiation at diffraction angles  $2\theta$  from 10° to 110° with a 0.02° step width. The data were analysed by Rietveld refinement using Fullprof software.<sup>40</sup>

$M(T)$  measurements for  $1.8 \text{ K} \leq T \leq 300 \text{ K}$  and  $M(H)$  measurements for  $H \leq 5.5 \text{ T}$  were carried out using a Quantum Design, Inc., Magnetic Properties Measurement System (MPMS). The high-temperature  $M(T)$  for  $300 \text{ K} \leq T \leq 900 \text{ K}$  was measured using the vibrating sample magnetometer (VSM) option of a Quantum Design, Inc., Physical Properties Measurement System (PPMS).  $C_p(T)$  data were obtained using a relaxation method with the heat capacity option of the PPMS. Four-probe  $\rho(T)$  data were obtained with an ac current amplitude  $I = 1 \mu\text{A}$  at a frequency of 37.7 Hz using the ac transport option of the PPMS. Electrical contacts to a crystal were made by soldering 0.05 mm diameter Pt wire to the crystal using indium solder.

## III. EXPERIMENTAL RESULTS

### A. Crystal structure

The crystal symmetry of several (Sr,Ca) $\text{Mn}_2\text{As}_2$  crystals was checked by x-ray Laue back scattering which showed trigonal symmetry with well-defined diffraction spots which clearly indicated the good quality of the crystals. In this paper we use the hexagonal setting for the trigonal unit cell. The data also revealed that (Sr,Ca) $\text{Mn}_2\text{As}_2$  crystals grow with a flat plate structure with the plate surface parallel to the hexagonal  $ab$  plane.

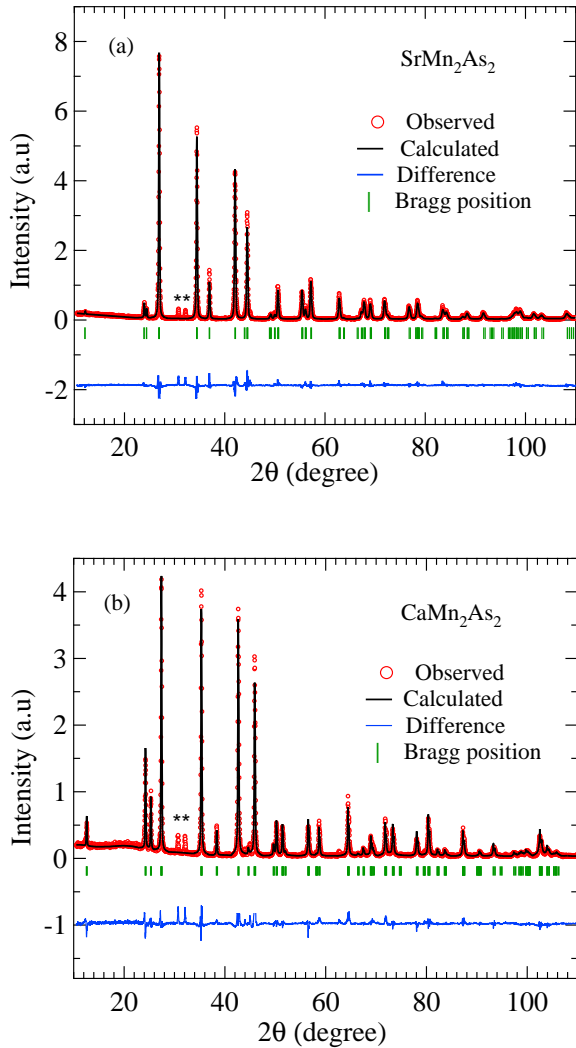


FIG. 1: (Colour online) Powder x-ray diffraction patterns (open circles) of (a)  $\text{SrMn}_2\text{As}_2$  and (b)  $\text{CaMn}_2\text{As}_2$  at room temperature. The solid line represents the Rietveld refinement fit calculated for the  $\text{CaAl}_2\text{Si}_2$ -type trigonal structure with space group  $P\bar{3}m1$ . The unindexed peaks marked with blue asterisks correspond to peaks from the elemental Sn flux.

SEM imaging and EDX analyses were performed to check the chemical composition and surface morphology of the crystals. The average elemental ratio of the samples was in agreement with the expected 1:2:2 stoichiometry of the compounds to within the errors. The amount of Sn incorporated into the crystal structure from the Sn flux is zero to within the experimental error. The present analyses did not show any other elements.

The phase purity of our  $(\text{Sr}, \text{Ca})\text{Mn}_2\text{As}_2$  crystals was confirmed by powder XRD. Their XRD patterns at 300 K along with the results of Rietveld refinements are shown in Figs. 1(a) and 1(b), respectively. The refinement results confirm that the crystals have the trigonal  $\text{CaAl}_2\text{Si}_2$ -type structure with space group  $P\bar{3}m1$ . The

TABLE I: Crystallographic and Rietveld refinement parameters obtained from powder XRD of  $\text{SrMn}_2\text{As}_2$  and  $\text{CaMn}_2\text{As}_2$  crystals. The atomic coordinates of  $(\text{Sr}, \text{Ca})\text{Mn}_2\text{As}_2$  are  $\text{Sr}/\text{Ca}$ : 1a (0, 0, 0); Mn: 2d  $(1/3, 2/3, z_{\text{Mn}})$ ; and As: 2d  $(1/3, 2/3, z_{\text{As}})$ . The shortest Mn–Mn interatomic distances in  $(\text{Sr}, \text{Ca})\text{Mn}_2\text{As}_2$  [see Fig. 2(b)] are also listed.

	$\text{SrMn}_2\text{As}_2$	$\text{CaMn}_2\text{As}_2$
Structure	$\text{CaAl}_2\text{Si}_2$ -type trigonal	$\text{CaAl}_2\text{Si}_2$ -type trigonal
Space group	$P\bar{3}m1$	$P\bar{3}m1$
Lattice parameters		
$a$ (Å)	4.2966(1)	4.2377(1)
$c$ (Å)	7.2996(2)	7.0333(2)
$c/a$	1.6989(1)	1.6597(1)
$V_{\text{cell}}$ (Å <sup>3</sup> )	116.700(6)	109.385(5)
Atomic coordinates		
$z_{\text{Mn}}$	0.6231(1)	0.6244(5)
$z_{\text{As}}$	0.2667(2)	0.2536(1)
Refinement quality		
$\chi^2$	4.66	4.81
$R_p$ (%)	6.13	10.8
$R_{wp}$ (%)	7.41	8.84
Shortest Mn–Mn distances (Å)		
$d_1$	3.063(1)	2.971(2)
$d_2$	4.297(2)	4.238(1)
$d_3$	5.271(3)	5.145(4)
$d_{z1}$	6.048(2)	5.872(3)
$d_{z2}$	7.299(4)	7.237(2)

refinement and crystal parameters obtained are listed in Table I. The latter parameters are in good agreement with previously reported values.<sup>31,32,36</sup>

Figure 2(a) shows a unit cell of trigonal  $\text{SrMn}_2\text{As}_2$  and  $\text{CaMn}_2\text{As}_2$  in the hexagonal setting. As shown in Figs. 2(b) and 2(d), the structure consists of corrugated honeycomb  $[\text{Mn}_2\text{As}_2]^{2-}$  layers that are stacked along the  $c$  axis and separated by  $\text{Sr}^{+2}$  or  $\text{Ca}^{+2}$  cations, respectively. Alternatively, the Mn sublattice can be viewed as triangular double layers of Mn stacked along the  $c$  axis and separated by Ca or Sr atoms. The three smallest Mn–Mn interatomic distances [see Fig. 2(b)] are within the corrugated Mn honeycomb layers and are listed in Table I. The nearest-neighbor Mn–Mn distance ( $d_1$ ) is between the two Mn atoms at different heights ( $z$  values) within a unit cell. The second-nearest-neighbor Mn–Mn distance ( $d_2$ ) is between Mn atoms at the same height in adjacent unit cells along the  $ab$  plane forming a triangular-lattice layer, and the third nearest-neighbor Mn–Mn distance ( $d_3$ ) is between nearest-neighbor Mn atoms in adjacent unit cells in the  $ab$  plane. The nearest- and second-nearest-neighbor distances  $d_{z1}$  and  $d_{z2}$  between Mn atoms in adjacent layers in different unit cells

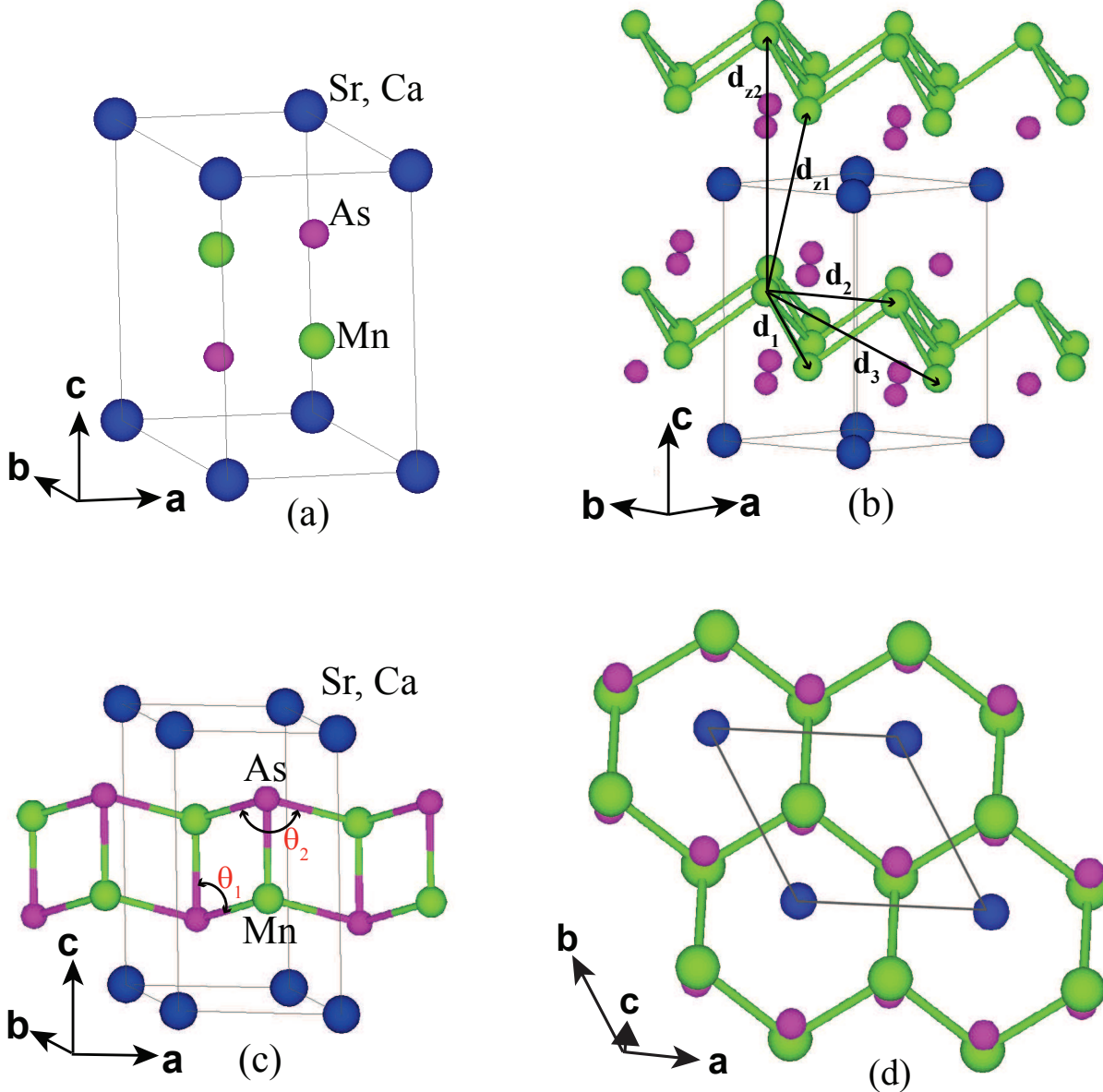


FIG. 2: (Colour online) Trigonal CaAl<sub>2</sub>Si<sub>2</sub>-type crystal structure of (Sr,Ca)Mn<sub>2</sub>As<sub>2</sub> in the hexagonal setting. (a) Outline of a unit cell containing one formula unit. (b) Corrugated Mn honeycomb layers as viewed from nearly perpendicular to the  $c$  axis. The smallest Mn–Mn interatomic distances within a corrugated Mn honeycomb layer ( $d_1$ ,  $d_2$ ,  $d_3$ ) and between layers ( $d_{z1}$ ,  $d_{z2}$ ) are indicated. (c) Expanded view of the structure from a view nearly perpendicular to the  $c$  axis showing the corrugated [Mn<sub>2</sub>As<sub>2</sub>]<sup>-2</sup> honeycomb layers separated by Sr or Ca. (d) Projection of the Mn sublattice onto the  $ab$ -plane with a slight  $c$  axis component illustrating the corrugated Mn honeycomb lattice. The corrugated honeycomb lattice layer can be viewed as a triangular lattice bilayer [compare with panel (b)]. The outline of a unit cell in the  $ab$ -plane is also shown.

along the  $c$  axis are also listed in Table I.

Since the minimum intralayer Mn–Mn distance  $d_1 \approx 3 \text{ \AA}$  is much shorter than the minimum interlayer Mn–Mn distance ( $d_{z1} \approx 6 \text{ \AA}$ ), CaMn<sub>2</sub>As<sub>2</sub> and SrMn<sub>2</sub>As<sub>2</sub> likely have a quasi-two-dimensional Mn–Mn exchange interaction connectivity. This large spatial anisotropy in the exchange interactions should be obvious from  $\chi(T > T_N)$  measurements, which is confirmed below. These exchange interactions could arise from direct Mn–Mn interactions and/or from indirect Mn–As–Mn superexchange

interactions. The latter would likely occur via two main paths: (i) between first-nearest-neighbor Mn spins with  $\angle \text{Mn-As-Mn}$  ( $\theta_1$ ) = 72° and another between second-neighbor Mn spins with  $\angle \text{Mn-As-Mn}$  ( $\theta_2$ ) = 111° [see Fig. 2(c)]. It will be interesting to see which of these interactions are dominant within the unusual trigonal symmetry of the Mn spin lattice.

To summarize, the (Sr,Ca)Mn<sub>2</sub>As<sub>2</sub> trigonal structure is quite different from the body-centered tetragonal ThCr<sub>2</sub>Si<sub>2</sub> structure found for the AFe<sub>2</sub>As<sub>2</sub> parent

compounds that is composed of metal-arsenide tetrahedra separated by alkaline earth layers. The primary difference between them is the geometry of the transition metal layers. In  $(\text{Sr}, \text{Ca})\text{Mn}_2\text{As}_2$ , the Mn bilayer is a corrugated Mn honeycomb lattice where each Mn atom is coordinated by three other Mn atoms at  $\sim 90^\circ$  like the corner of the cube as seen in Figs. 2(b) and 2(c), whereas in  $\text{ThCr}_2\text{Si}_2$ -type compounds such as  $\text{BaMn}_2\text{As}_2$  or  $\text{BaFe}_2\text{As}_2$ , the Mn or Fe network is a simple square-planar lattice where each Mn or Fe is coordinated by four other Mn or Fe atoms, also at  $90^\circ$  angles between them. On the other hand, the AFM in  $\text{BaMn}_2\text{As}_2$  is quasi-two-dimensional,<sup>21</sup> just as we find it to be in  $(\text{Sr}, \text{Ca})\text{Mn}_2\text{As}_2$  from the  $\chi(T)$  data in Sec. III C below.

### B. In-Plane Electrical Resistivity

Figures 3(a) and 3(b) show  $\rho(T)$  of  $\text{SrMn}_2\text{As}_2$  and  $\text{CaMn}_2\text{As}_2$ , respectively, from  $\sim 50$  to  $300$  K measured in the  $ab$  plane. The data show that both compounds are semiconductors with insulating intrinsic ground states. We fitted  $\rho(T)$  in the temperature region between  $70$  and  $120$  K by the expression  $\log_{10} \rho = A + 2.303\Delta/k_B T$ , where  $A$  is a constant,  $k_B$  is Boltzmann's constant and  $\Delta$  is the activation energy. The fits are shown as the solid straight lines through the data in the insets of Figs. 3(a) and 3(b), which give the activation energies  $\Delta = 85$  meV for  $\text{SrMn}_2\text{As}_2$  and  $\Delta = 61$  meV for  $\text{CaMn}_2\text{As}_2$ . These activation energies are of the same order as previously obtained from  $\rho(T)$  data for  $\text{BaMn}_2\text{As}_2$ .<sup>19</sup> Our activation energy for  $\text{SrMn}_2\text{As}_2$  is significantly smaller than the previously reported values  $\Delta = 0.29$  and  $0.64$  eV, depending on the  $T$  range, that were also obtained from single-crystal in-plane  $\rho(T)$  data.<sup>36</sup>

### C. Magnetization and Magnetic Susceptibility

The zero-field-cooled (ZFC) magnetic susceptibility  $\chi \equiv M/H$  versus  $T$  measured in  $H = 0.1$  T and  $H = 3$  T applied in the  $ab$  plane ( $H \parallel ab$ ,  $\chi_{ab}$ ) and along the  $c$  axis ( $H \parallel c$ ,  $\chi_c$ ) for single crystals of  $\text{SrMn}_2\text{As}_2$  and  $\text{CaMn}_2\text{As}_2$  are shown in Figs. 4 and 5, respectively.

Clear AFM transitions are observed in  $\chi(T)$  at  $T_N \approx 120$  K for  $\text{SrMn}_2\text{As}_2$  and  $T_N \approx 65$  K for  $\text{CaMn}_2\text{As}_2$ , as indicated by vertical arrows in Figs. 4(a) and 5(a), respectively. We also performed FC (field-cooled) and ZFC  $\chi(T)$  measurements at  $H = 0.1$  T and  $H = 3$  T (not shown here). No hysteresis was observed between the ZFC and FC data, which is consistent with long-range AFM ordering of  $(\text{Sr}, \text{Ca})\text{Mn}_2\text{As}_2$  below their respective Néel temperatures. The data in Figs. 4(a) and 5(a) for  $T > T_N$  are nearly isotropic, as expected for  $\text{Mn}^{+2}$  with spin  $S = 5/2$  and  $g \approx 2$ .

From Figs. 4(a) and 5(a), the anisotropy in  $\chi$  at  $T < T_N$  indicates that the hard axis is the  $c$  axis and the  $ab$  plane is the easy plane for both compounds. Further-

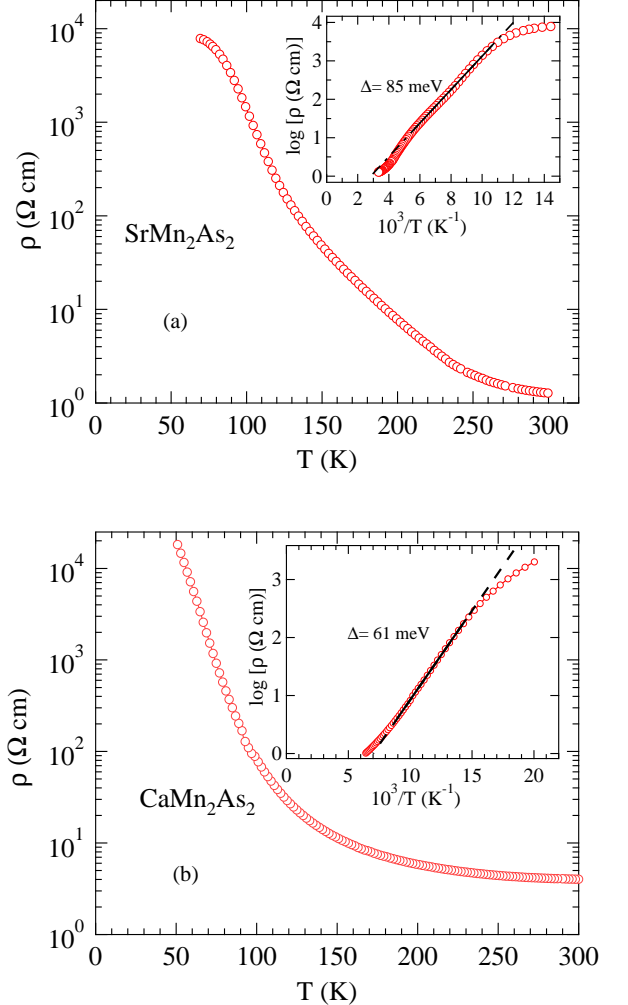


FIG. 3: (Colour online) In-plane electrical resistivity  $\rho$  of (a)  $\text{SrMn}_2\text{As}_2$  and (b)  $\text{CaMn}_2\text{As}_2$  versus temperature  $T$  from  $\sim 50$  to  $300$  K. The insets show plots of  $\log_{10} \rho$  versus  $1000/T$ . The solid straight lines through the data are fits over the temperature interval between  $70$  and  $120$  K by the expression  $\log_{10} \rho = A + 2.303\Delta/T$  and the resulting fitted activation energies are listed. The dashed lines are extrapolations.

more, the nonzero limits of  $\chi_{ab}(T \rightarrow 0)$  suggest that the AFM structure could be either a collinear AFM with multiple domains aligned within the  $ab$  plane or an intrinsic noncollinear structure with moments again aligned in the  $ab$  plane.<sup>41–44</sup> In  $\text{SrMn}_2\text{As}_2$  [see Fig. 4(b)], the anisotropy in  $\chi$  for  $T < T_N$  is eliminated by a field of  $3$  T, which indicates a relatively small magnetocrystalline anisotropy compared to that in  $\text{CaMn}_2\text{As}_2$  judging from Fig. 5(b). The small upturns in  $\chi$  in Figs. 4 and 5 below  $\sim 20$  K are believed due to trace amounts of paramagnetic local-moment impurities.

A small jump in  $\chi(T)$  is observed for  $\text{SrMn}_2\text{As}_2$  in Fig. 4(b) on cooling below about  $320$  K. This is believed due to FM MnAs impurities with this Curie temperature

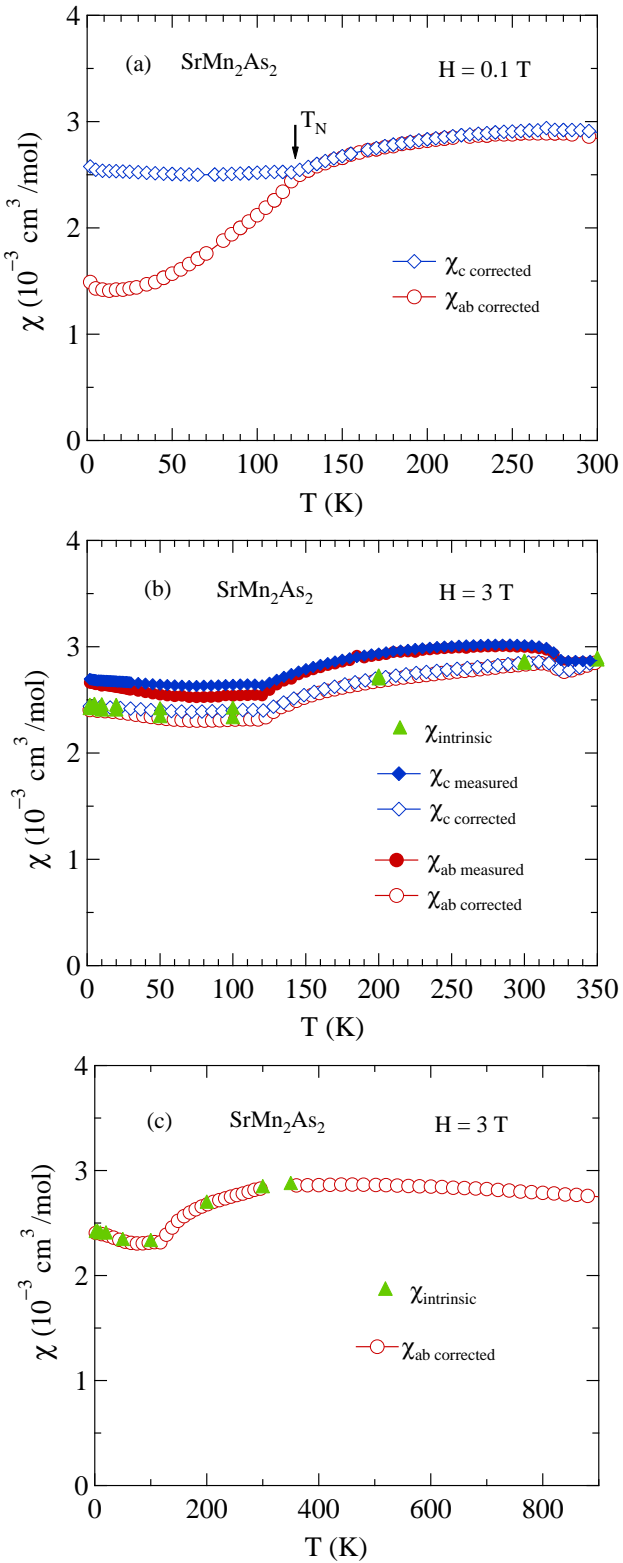


FIG. 4: (Color online) ZFC magnetic susceptibility  $\chi(T)$  of  $\text{SrMn}_2\text{As}_2$  from 1.8 to 300 K measured in a magnetic field (a)  $H = 0.1 \text{ T}$  and (b)  $H = 3 \text{ T}$  applied in the  $ab$  plane ( $H \parallel ab$ ,  $\chi_{ab}$ ) and along the  $c$  axis ( $H \parallel c$ ,  $\chi_c$ ). (c) ZFC susceptibility versus  $T$  for  $1.8 \leq T \leq 900 \text{ K}$  measured in  $H = 3 \text{ T}$  applied in the  $ab$  plane ( $H \perp c$ ). The “intrinsic” values are obtained from  $M(H)$  isotherms using Eq. (1) and the “corrected” ones are obtained from  $M(T)$  data using Eq. (2).

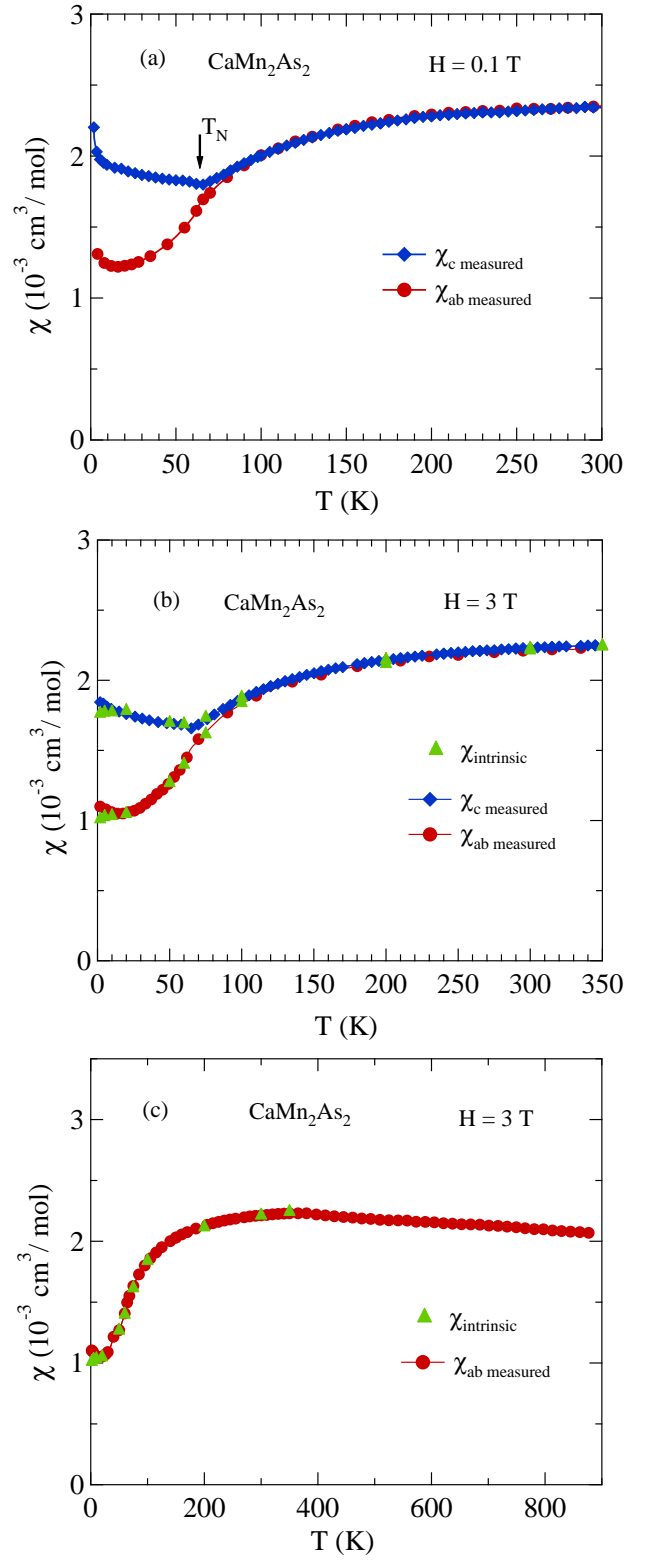


FIG. 5: (Color online) Magnetic susceptibility data for  $\text{CaMn}_2\text{As}_2$ . The plot and symbol designations are the same as for  $\text{SrMn}_2\text{As}_2$  in Fig. 4.

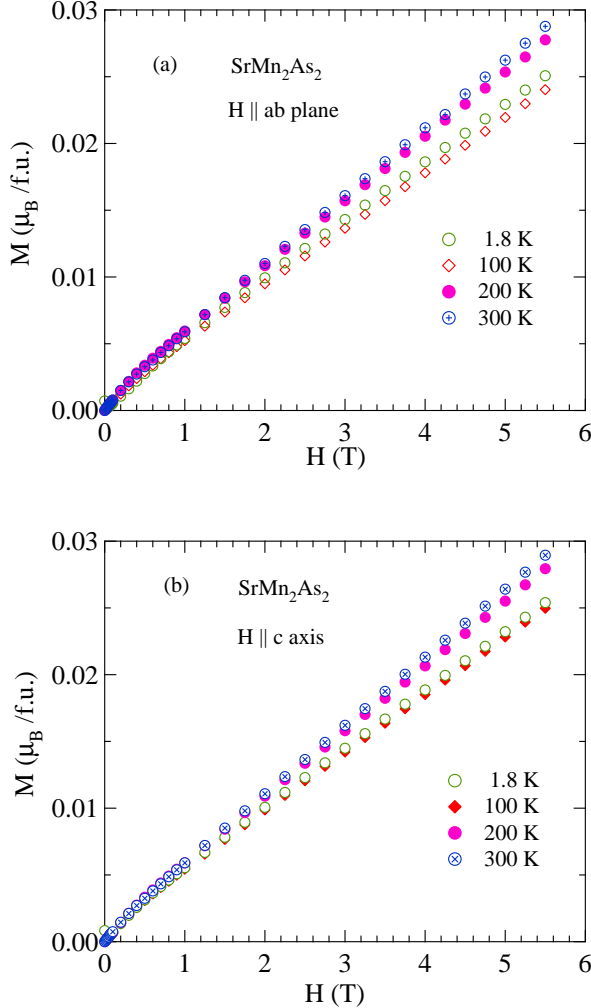


FIG. 6: (Color online) Magnetization  $M$  versus magnetic field  $H$  at various temperatures  $T$  with (a)  $H$  in the  $ab$  ( $H \perp c$ ) plane and with (b)  $H$  along  $c$  axis ( $H \parallel c$ ) for  $\text{SrMn}_2\text{As}_2$ .

that are present on the crystal surface and/or as an inclusion in the crystal, as previously observed for  $\text{BaMn}_2\text{As}_2$  crystals.<sup>19</sup> To extract the intrinsic magnetic behavior of  $\text{SrMn}_2\text{As}_2$ , we carried out  $M(H)$  isotherm measurements at various temperatures. Figures 6 and 7 show isothermal  $M(H)$  data for  $\text{SrMn}_2\text{As}_2$  and  $\text{CaMn}_2\text{As}_2$  crystals, respectively, at different  $T$  for  $H \parallel ab$  plane ( $M_{ab}$ ) and  $H \parallel c$  axis ( $M_c$ ). The  $M(H)$  curves are almost linear at high fields, but one sees nonlinearities at low fields ( $H < 1\text{--}2$  T) for  $T < 200$  K, confirming the presence of saturable FM impurities.

To extract the intrinsic  $\chi$  ( $\chi_{\text{int}}$ ) we fitted the  $M(H)$  data in the high-field range  $H = 3.5\text{--}5.5$  T by the linear relation

$$M(H, T) = M_s(T) + \chi_{\text{int}}(T)H, \quad (1)$$

where  $M_s(T)$  is the saturation magnetization due to the FM impurities. The  $T \rightarrow 0$  value of  $M_s$  for  $\text{SrMn}_2\text{As}_2$

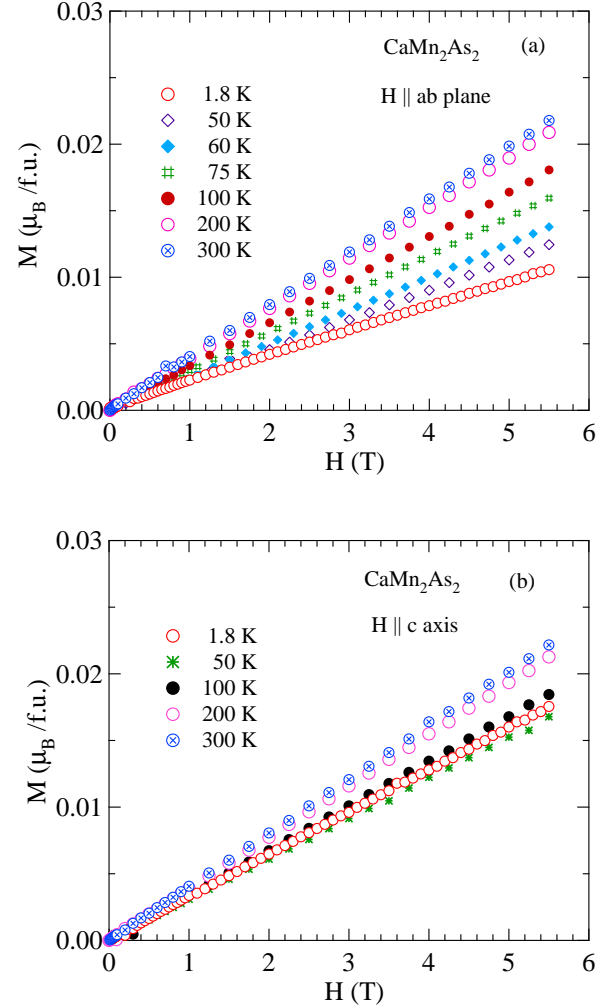


FIG. 7: (Color online) Magnetization  $M$  versus magnetic field  $H$  at various temperatures  $T$  with (a)  $H$  in the  $ab$  ( $H \parallel ab$ ) plane and with (b)  $H$  along  $c$  axis ( $H \parallel c$ ) for  $\text{CaMn}_2\text{As}_2$ .

is  $7 \text{ G cm}^3/\text{mol} = 0.0013 \mu_{\text{B}}/\text{f.u.}$ , which corresponds to  $0.04 \text{ mol\%}$  of MnAs impurities using the saturation moment of  $\approx 3.5 \mu_{\text{B}}/\text{f.u.}$  (Refs. 45,46) for MnAs. The  $\chi(T) \equiv M(T)/H$  data in Figs. 4(b) and 5(b) were measured with  $H = 3$  T. Therefore, we obtained the intrinsic  $\chi$  from the isotherm data according to

$$\chi_{\text{int}}(T) = \frac{M_{\text{measured}}(T) - M_s(T)}{3 \text{ T}}. \quad (2)$$

The  $\chi_{\text{int}}(T)$  data are shown by the filled green triangles in Figs. 4(b) and 5(b). It is seen that the  $\chi_{\text{int}}(T)$  data for  $\text{CaMn}_2\text{As}_2$  match very well for both field directions with the  $\chi \equiv M/H$  data in Fig. 5(b), indicating a clean crystal without any detectable FM impurities.

In order to further clarify the magnetism in these systems we measured  $\chi(T) \equiv M(T)/H$  in the extended temperature range up to 900 K for  $(\text{Sr}, \text{Ca})\text{Mn}_2\text{As}_2$  as shown in Figs. 4(c) and 5(c), respectively. One sees that

$\chi$  exhibits very broad maxima at  $\sim 400$  K for both compounds. This feature is a signature of a low-dimensional local-moment AFM system.<sup>21</sup> Thus  $(\text{Sr}, \text{Ca})\text{Mn}_2\text{As}_2$  undergo a phase transition to a long-range ordered state below  $T_N$ , preceded by strong short-range AFM order at higher temperatures. Indeed, the Curie-Weiss temperature region of  $\chi$  is not reached even at 900 K, indicating that strong AFM correlations survive to significantly higher temperatures.

From the Mn-Mn interatomic distances discussed in Sec. III A, we inferred that the Mn-Mn exchange coupling along the  $c$  axis between the corrugated honeycomb Mn layers in the  $ab$  plane is much smaller than within the layers. We confirm this here and in addition infer that the Mn-Mn exchange coupling within the corrugated honeycomb layers is dominantly antiferromagnetic.

#### D. Heat Capacity

Figures 8(a) and 8(b) show zero-field  $C_p(T)$  data for  $\text{SrMn}_2\text{As}_2$  and  $\text{CaMn}_2\text{As}_2$ , respectively. The sharp anomalies in  $C_p(T)$  at  $120(2)$  K in  $\text{SrMn}_2\text{As}_2$  and at  $62(3)$  K in  $\text{CaMn}_2\text{As}_2$  are the respective Néel temperatures of the two compounds, which are in good agreement with respective  $T_N$  values found in the  $\chi(T)$  data.

The insets of Figs. 8(a) and 8(b) show  $C_p(T)/T$  versus  $T^2$  between 1.8 and 5 K. The data were fitted by the expression

$$\frac{C_p}{T} = \gamma + \beta T^2, \quad (3)$$

where the coefficient  $\gamma$  is usually due to the electronic contribution (Sommerfeld coefficient) and  $\beta$  reflects the lattice contribution in the absence of AFM contributions. From the fits of Eq. (4) to the data in the insets of Figs. 8(a) and 8(b) we obtain  $\gamma = 0.0(1)$  mJ/(mol K $^2$ ) for  $\text{SrMn}_2\text{As}_2$  and  $0.05(7)$  mJ/(mol K $^2$ ) for  $\text{CaMn}_2\text{As}_2$ . The null values of  $\gamma$  are consistent with the insulating ground states found from the  $\rho(T)$  measurements in Sec. III B.

The fitted values for  $\beta$  are  $0.35(1)$  mJ/(mol K $^4$ ) for  $\text{SrMn}_2\text{As}_2$  and  $0.37(1)$  mJ/(mol K $^4$ ) for  $\text{CaMn}_2\text{As}_2$ . We estimate the Debye temperatures  $\theta_D$  for the two compounds from the Debye theory according to

$$\theta_D = \left( \frac{12\pi^4 R n}{5\beta} \right)^{1/3} \quad (4)$$

where  $R$  is the molar gas constant and  $n$  is the number of atoms per formula unit [ $n = 5$  for  $(\text{Sr}, \text{Ca})\text{Mn}_2\text{As}_2$ ]. We obtain  $\theta_D = 303(3)$  K and  $297(3)$  K for  $\text{SrMn}_2\text{As}_2$  and  $\text{CaMn}_2\text{As}_2$ , respectively. In the absence of anisotropy gaps in the AFM spin-wave spectrum, contributions to  $\beta$  could arise from excitations of three-dimensional AFM spin waves at the low temperatures at which the  $\beta$  values were extracted; hence the quoted values of  $\theta_D$  are lower limits.

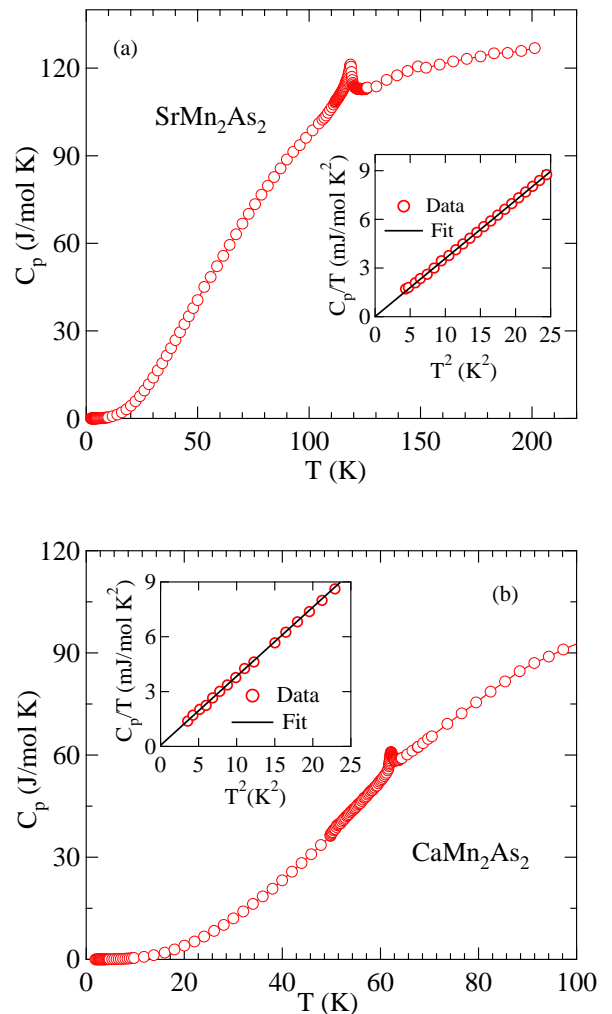


FIG. 8: (Color online) Heat capacity  $C_p$  versus temperature  $T$  for (a)  $\text{SrMn}_2\text{As}_2$  and (b)  $\text{CaMn}_2\text{As}_2$ . The insets show  $C_p(T)/T$  versus  $T^2$  for  $T < 5$  K, where the straight lines through the respective data are fits by Eq. (3).

#### IV. SUMMARY

We have shown that  $\text{SrMn}_2\text{As}_2$  and  $\text{CaMn}_2\text{As}_2$  are AFM insulators with Néel temperatures  $T_N = 120$  K and  $62$  K, respectively. The microscopic origin of this large difference in magnitude of the Néel temperatures together with the reason why the Sr compound has a higher  $T_N$  than the Ca one, in spite of the smaller unit cell, remain to be explained.

The  $\chi(T)$  data at  $T \leq T_N$  indicate that the hexagonal  $c$  axis is a hard axis, with the ordered Mn spin-5/2 moments lying within the  $ab$  plane. Since a collinear AFM structure within the  $ab$  plane is inferred from neutron diffraction measurements that were carried out in a companion study,<sup>39</sup> the nonzero limits of  $\chi_{ab}(T < T_N)$  observed for the two compounds must arise from the

three collinear AFM domains with the axes at  $60^\circ$  to each other within the  $ab$  plane. If the populations of the three domains are equal, within molecular field theory one obtains  $\chi_{ab}(T \rightarrow 0) = \chi(T_N)/2$ , in approximate agreement with the  $\chi_{ab}(T)$  data in Figs. 4(a) and 5(a). Our calculation of the easy axis predicted by the Mn–Mn magnetic dipole interactions in a collinear magnetic structure of  $\text{SrMn}_2\text{As}_2$  using the formalism of Ref. 47 and the experimental crystal structure predicts that the ordered moments should lie in the  $ab$  plane as observed<sup>39</sup> in the neutron diffraction experiments.

Thus the potential geometric frustration for AFM ordering within the triangular-lattice bilayers parallel to the  $ab$  plane that originally motivated this work is apparently not realized in  $\text{SrMn}_2\text{As}_2$  and  $\text{CaMn}_2\text{As}_2$ . In particular, if AFM Mn–Mn exchange interactions within a triangular sublattice layer were dominant, a noncollinear AFM structure would have resulted instead of the observed collinear AFM structure.<sup>39</sup> On the other hand, the strong dynamic AFM short-range correlations up

to at least 900 K as reflected in our  $\chi(T)$  measurements of both compounds are evidently due to quasi-two-dimensional connectivity of strong AFM Mn–Mn exchange interactions within the corrugated honeycomb Mn layers. This in turn offers the possibility of interesting electronic ground states arising upon doping these materials into the metallic state.

## Acknowledgments

We thank P. Das, A. Kreyssig and A. I. Goldman for helpful discussions. This research was supported by the U.S. Department of Energy, Office of Basic Energy Sciences, Division of Materials Sciences and Engineering. Ames Laboratory is operated for the U.S. Department of Energy by Iowa State University under Contract No. DE-AC02-07CH11358.

\* Present address: Department of Physics and Astronomy, Louisiana State University, Baton Rouge, Louisiana 70803, USA

† Electronic address: johnston@ameslab.gov

<sup>1</sup> G. Just and P. Paufler, *J. Alloys Compd.* **232**, 1 (1996).

<sup>2</sup> D. C. Johnston, *Adv. Phys.* **59**, 803 (2010).

<sup>3</sup> G. R. Stewart, *Rev. Mod. Phys.* **83**, 1589 (2011).

<sup>4</sup> D. J. Scalapino, *Rev. Mod. Phys.* **84**, 1383 (2012).

<sup>5</sup> E. Dagotto, *Rev. Mod. Phys.* **85**, 849 (1993).

<sup>6</sup> R. M. Fernandes, A. V. Chubukov, and J. Schmalian, *Nat. Phys.* **10**, 97 (2014).

<sup>7</sup> H. Hosono and K. Kuroki, *Physica C* **514**, 399 (2015).

<sup>8</sup> P. Dai, *Rev. Mod. Phys.* **87**, 855 (2015).

<sup>9</sup> D. S. Inosov, *Compt. Rend. Phys.* **17**, 60 (2016).

<sup>10</sup> Q. Si, R. Yu, and E. Abrahams, *Nat. Rev. Mater.* **1**, 1 (2016).

<sup>11</sup> E. D. Bauer, F. Ronning, B. L. Scott, and J. D. Thompson, *Phys. Rev. B* **78**, 172504 (2008).

<sup>12</sup> F. Ronning, N. Kurita, E. D. Bauer, B. L. Scott, T. Park, T. Klimczuk, R. Movshovich, and J. D. Thompson, *J. Phys.: Condens. Matter* **20**, 342203 (2008).

<sup>13</sup> A. Pandey, D. G. Quirinale, W. Jayasekara, A. Sapkota, M. G. Kim, R. S. Dhaka, Y. Lee, T. W. Heitmann, P. W. Stephens, V. Oglablichev, A. Kreyssig, R. J. McQueeney, A. I. Goldman, A. Kaminski, B. N. Harmon, Y. Furukawa, and D. C. Johnston, *Phys. Rev. B* **88**, 014526 (2013).

<sup>14</sup> W. Jayasekara, Y. Lee, A. Pandey, G. S. Tucker, A. Sapkota, J. Lamsal, S. Calder, D. L. Abernathy, J. L. Niedziela, B. N. Harmon, A. Kreyssig, D. Vaknin, D. C. Johnston, A. I. Goldman, and R. J. McQueeney, *Phys. Rev. Lett.* **111**, 157001 (2013).

<sup>15</sup> P. Wiecki, V. Oglablichev, A. Pandey, D. C. Johnston, and Y. Furukawa, *Phys. Rev. B* **91**, 220406(R) (2015).

<sup>16</sup> A. S. Sefat, D. J. Singh, R. Jin, M. A. McGuire, B. C. Sales, and D. Mandrus, *Phys. Rev. B* **79**, 024512 (2009).

<sup>17</sup> V. K. Anand, D. G. Quirinale, Y. Lee, B. N. Harmon, Y. Furukawa, V. V. Oglablichev, A. Huq, D. L. Abernathy, P.

W. Stephens, R. J. McQueeney, A. Kreyssig, A. I. Goldman, and D. C. Johnston, *Phys. Rev. B* **90**, 064517 (2014).

<sup>18</sup> P. Wiecki, B. Roy, D. C. Johnston, S. L. Bud'ko, P. C. Canfield, and Y. Furukawa, *Phys. Rev. Lett.* **115**, 137001 (2015).

<sup>19</sup> Y. Singh, A. Ellern, and D. C. Johnston, *Phys. Rev. B* **79**, 094519 (2009).

<sup>20</sup> Y. Singh, M. A. Green, Q. Huang, A. Kreyssig, R. J. McQueeney, D. C. Johnston, and A. I. Goldman, *Phys. Rev. B* **80**, 100403(R) (2009).

<sup>21</sup> D. C. Johnston, R. J. McQueeney, B. Lake, A. Honecker, M. E. Zhitomirsky, R. Nath, Y. Furukawa, V. P. Antropov, and Y. Singh, *Phys. Rev. B* **84**, 094445 (2011).

<sup>22</sup> A. Antal, T. Knoblauch, Y. Singh, P. Gegenwart, D. Wu, and M. Dressel, *Phys. Rev. B* **86**, 014506 (2012).

<sup>23</sup> S. Calder, B. Saparov, H. B. Cao, J. L. Niedziela, M. D. Lumsden, A. S. Sefat, and A. D. Christianson, *Phys. Rev. B* **89**, 064417 (2014).

<sup>24</sup> A. Pandey, R. S. Dhaka, J. Lamsal, Y. Lee, V. K. Anand, A. Kreyssig, T. W. Heitmann, R. J. McQueeney, A. I. Goldman, B. N. Harmon, A. Kaminski, and D. C. Johnston, *Phys. Rev. Lett.* **108**, 087005 (2012).

<sup>25</sup> S. Yeninas, A. Pandey, V. Oglablichev, K. Mikhalev, D. C. Johnston, and Y. Furukawa, *Phys. Rev. B* **88**, 241111(R) (2013).

<sup>26</sup> J.-K. Bao, H. Jiang, Y.-L. Sun, W.-H. Jiao, C.-Y. Shen, H.-J. Guo, Y. Chen, C.-M. Feng, H.-Q. Yuan, Z.-A. Xu, G.-H. Cao, R. Sasaki, T. Tanaka, K. Matsubayashi, and Y. Uwatoko, *Phys. Rev. B* **85**, 144523 (2012).

<sup>27</sup> A. Pandey, B. G. Ueland, S. Yeninas, A. Kreyssig, A. Sapkota, Yang Zhao, J. S. Helton, J. W. Lynn, R. J. McQueeney, Y. Furukawa, A. I. Goldman, and D. C. Johnston, *Phys. Rev. Lett.* **111**, 047001 (2013).

<sup>28</sup> B. G. Ueland, A. Pandey, Y. Lee, A. Sapkota, Y. Choi, D. Haskel, R. A. Rosenberg, J. C. Lang, B. N. Harmon, D. C. Johnston, A. Kreyssig, and A. I. Goldman, *Phys. Rev. Lett.* **114**, 217001 (2015).

<sup>29</sup> A. Pandey and D. C. Johnston, Phys. Rev. B **92**, 174401 (2015).

<sup>30</sup> J. Lamsal, G. S. Tucker, T. W. Heitmann, A. Kreyssig, A. Jesche, A. Pandey, W. Tian, R. J. McQueeney, D. C. Johnston, and A. I. Goldman, Phys. Rev. B **87**, 144418 (2013).

<sup>31</sup> A. Mewis, Z. Naturforsch. **33b**, 606 (1978).

<sup>32</sup> E. Brechtel, G. Cordier, and H. Schäfer, Z. Naturforsch. **33b**, 820 (1978).

<sup>33</sup> A. P. Ramirez, Annu. Rev. Mater. Sci. **24**, 453 (1994).

<sup>34</sup> R. Moessner and A. P. Ramirez, Physics Today **59**, 24 (2006).

<sup>35</sup> L. Balents, Nature **464**, 199 (2010).

<sup>36</sup> Z.W. Wang, H.X. Yang, H.F. Tian, H.L. Shi, J.B. Lu, Y.B. Qin, Z. Wang, J.Q. Li, J. Phys. Chem. Solids **72**, 457 (2011).

<sup>37</sup> W. Ratcliff II, A. L. Lima Sharma, A. M. Gomes, J. L. Gonzalez, Q. Huang, and J. Singleton, J. Magn. Magn. Mater. **321**, 2612 (2009).

<sup>38</sup> C. A. Bridges, V. V. Krishnamurthy, S. Poulton, M. P. Paranthaman, B. C. Sales, C. Myers, and S. Bobev, J. Magn. Magn. Mater. **321**, 2653 (2009).

<sup>39</sup> P. Das, N. S. Sangeetha, A. Pandey, Z. A. Benson, T. W. Heitmann, D. C. Johnston, A. I. Goldman, and A. Kreyssig, (unpublished).

<sup>40</sup> J. Rodríguez-Carvajal, Phys. B: Condens. Matter **192**, 55 (1993).

<sup>41</sup> D. C. Johnston, Phys. Rev. Lett. **109**, 077201 (2012).

<sup>42</sup> D. C. Johnston, Phys. Rev. B **91**, 064427 (2015).

<sup>43</sup> V. K. Anand and D. C. Johnston, Phys. Rev. B **91**, 184403 (2015).

<sup>44</sup> D. H. Ryan, J. M. Cadogan, V. K. Anand, D. C. Johnston, and R. Flacau, J. Phys.: Condens. Matter **27**, 206002 (2015).

<sup>45</sup> S. Haneda, N. Kazama, Y. Yamaguchi, and H. Watanabe, J. Phys. Soc. Jpn. **42**, 1201 (1977).

<sup>46</sup> B. Saparov, J. E. Mitchell, and A. S. Sefat, Supercond. Sci. Technol. **25**, 084016 (2012).

<sup>47</sup> D. C. Johnston, Phys. Rev. B **93**, 014421 (2016).